Photonic crystal patterning of luminescent sol-gel films for light extraction

Amélie Revaux, Géraldine Dantelle, D. Decanini, François Guillemot, A. M. Haghiri-Gosnet, C. Weisbuch, Jean-Pierre Boilot, Thierry Gacoin, Henri Benisty

Photonic crystal patterning of luminescent sol–gel films for light extraction

Amelie Revaux[1], Geraldine Dantelle[1], Dominique Decanini[2], Francois Guillemot[1], Anne-Marie Haghiri-Gosnet[2], Claude Weisbuch[1], Jean-Pierre Boilot[1], Thierry Gacoin[1] and Henri Benisty[3]

[1] Laboratoire de Physique de la Matière Condensée, Ecole Polytechnique/CNRS UMR7643, F-91128 Palaiseau, France
[2] Laboratoire de Photonique et Nanostructures, CNRS UPR20, F-91460 Marcoussis, France
[3] Laboratoire Charles Fabry de l'Institut d'Optique, CNRS, Université Paris-Sud, Campus Polytechnique, RD 128, F-91127 Palaiseau Cedex, France

E-mail: amelie.revaux@polytechnique.edu

Abstract
Structured luminescent thin films are investigated in the context of improved light extraction of phosphors for solid-state-lighting applications. Thin films composed of a sol–gel titania matrix doped with europium chelates are studied as a model system. These films, patterned with a square photonic lattice by soft nanoimprint lithography, are characterized by angle-resolved fluorescence. Modeling of this simple technique is shown to fit well the experimental data, revealing in great detail the guided modes of the film and their extraction parameters. An eightfold extraction enhancement factor of the film emission is measured. To further improve the extraction efficiency, we investigate the role of an additional low-index mesoporous silica underlayer through its influence on the guided modes of different polarizations and their interactions with the photonic crystal. Results obtained on model systems open the way towards the optimization of light-emitting devices, using a strategy of dielectric microstructure engineering using the sol–gel process.

1. Introduction

In many examples of photo-active coatings involving light excitation and/or emission, the control of light propagation is an important issue that needs to be addressed in order to optimize the efficiency of the device. In the case, for example, of light-emitting devices such as OLEDS or GaN LEDs, light is emitted from a medium with a high refractive index, so that only a small fraction of the total light emitted inside a thin film is extracted because of total internal reflections inherent in the planar geometry. This fraction is evaluated to a mere $1/4n^2 \sim 10\%$ per face for films with a refractive index $n = 1.65$. Various approaches are used to address the extraction issue, such as the modification of substrate geometry to facilitate the escape of the trapped substrate modes [1] or the roughening of the emitting device surface [2]. Recently, the introduction of a periodic pattern, also termed a two-dimensional photonic crystal (PhC), has also been proposed as a deterministic way to extract light trapped in high-index guided modes of phosphor materials [3]. This approach has been widely studied in the case of GaN LEDs [4], OLEDs [5]. Some directional enhancement has also been observed by Mele *et al* for patterned conjugated polymers [6]. Several groups [7, 8] reported significant enhancement in fluorescence from quantum dots deposited on the surface of a 2D PhC (not inside the layer). PhC patterning also induces emission directionality so that, for example, in Ganesh's paper [7], a typical scanner solid angle collection leads to relatively high extraction enhancements ($\times$13). Lemarchand *et al* [9] have reported a $\times$2.5 enhancement of the angular-integrated luminescence of europium chelates inserted between high-

index oxide coatings that were further patterned into such a PhC, and they essentially assessed the directionality aspects.

Sol–gel chemistry has emerged as a promising method with a unique effectiveness for low cost deposition of thin oxide layers on arbitrary substrates. For optical applications, this process allows control of refractive index and thickness, and allows easy dispersion of optically active compounds (molecules, nanoparticles, etc) into the dielectric inorganic or organic/inorganic matrices. This has led to various applications such as waveguides [10], photochromic coatings, lasers, etc [11].

The idea developed in this work is to use the potentiality of the sol–gel process to investigate in more detail light extraction issues on model films patterned with 2D periodic structures. We here focused our attention on model luminescent films deposited on glass substrates and doped with europium chelates as molecular phosphors. These small-size molecular complexes possess a good quantum yield (25%) and are also easily incorporated into sol–gel films without any concentration quenching effect even at high loading fraction. Although europium chelates are not perfectly stable under excitation, they present the critical advantage of not inducing any microstructure (no light scattering) so that we can focus on the sole optical effect of the structuring of the film itself. Excitation and emission bands of chelates are also spectrally well separated, a premium for optical measurements. This large Stokes shift and the small absorption cross section of the chelate at its emission peaks discard reabsorption losses in the waveguide and ensure long propagation distances.

Extraction by a 2D PhC patterning mainly concerns the fraction of light that is guided in the slab rather than emitted towards the substrate. This approach is thus well adapted for light-emitting films with a high refractive index material. Amorphous TiO_2 films present a higher refractive index than hydrogels that have been previously patterned by soft lithography [12], which is an advantage in the context of light extraction. Titania-based sol–gel films were chosen with a refractive index limited to $n \sim 1.7$ instead of 2.2 or more, as could be expected from crystalline TiO_2. This is justified by the large increase of scattering losses that are found when crystallizing the TiO_2 through annealing, associated with a higher photo-degradation of luminescent chelates in this case.

In this configuration, before patterning of the doped TiO_2 film, one can easily estimate that 20% of the emitted light is extracted from the structure while 42% is guided into the TiO_2 film and 38% is guided into the glass substrate. Contrary to the modes guided within the TiO_2 luminescent films, the modes guided in the substrate cannot be extracted by the surface PhC due to their small optical overlap with the PhC. They thus exit from the edge of the sample and are lost for upper-face-emitting devices. One possibility we investigate in this work is to use a buffer layer with a low refractive index between the substrate and the TiO_2 film. We here take advantage of sol–gel chemistry that allows the elaboration of films with refractive indexes as low as 1.16 [13]. In this case, 20% of the emitted light is extracted from the structure while 72% is guided in the TiO_2 film and 8% is guided in the glass substrate. Starting from these films (i.e. with and without a low refractive index buffer), soft nanoimprint lithography (S-NIL) [14] is used for patterning a top TiO_2 layer with a simple square PhC. This structure is chosen so that emission from the chelates is spectrally and spatially coupled to the resonant modes of the photonic crystal and the guided light is extracted via leaky modes to free space. Our study first emphasizes generic properties of our structured films based on standard methods (SEM, AFM, standard spectrometry, etc). Second, a one-dimensional variant of angle-resolved fluorescence measurements is employed to investigate the way the guided mode interacts with the periodic pattern. Experimental results are discussed in relation to simulations of light propagation properties in order to clarify the effect of patterning and the role of the porous buffer layer on guided light and on its extraction.

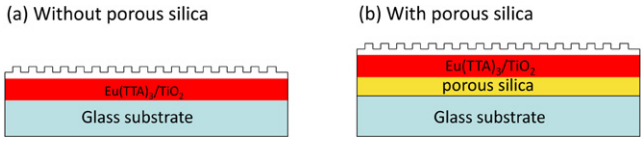

Figure 1. Sample structure. The first layer, deposited directly on the substrate (a) or on an intermediate porous silica layer (b), is the luminescent slab of TiO_2 doped with europium chelates. A second TiO_2 layer is deposited on top and patterned by soft nanoimprint lithography.

2. Structure and basic experiments

2.1. Photonic crystal properties

The waveguide is a sol–gel matrix of TiO_2 containing europium chelates as luminescent molecules. First, the europium titania precursor solution is deposited by spin-coating. Then, a second TiO_2 layer is deposited and patterned by soft nanoimprint lithography (S-NIL) [14]. Without annealing, the refractive index of the resulting film is around $n = 1.65$–1.7. It increases to $n = 2$ after annealing at 400 °C. Nevertheless, this annealing induces crystallization of the matrix, which leads to scattering of the light due to grain boundaries and the calcination of the Eu-complex ligands, which are responsible for the absorption of light and transfer to the europium. We thus study here amorphous films dried at 110 °C, with a thickness of about 280 nm and a refractive index of 1.65. The geometry of the investigated sample is presented in figure 1(a).

The SEM photograph in figure 2(a) shows the photonic architecture chosen for this study: a square photonic crystal with an air filling factor $f \approx 0.26$ and a period $a = 400$ nm. As discussed later in the text, this structure is appropriate for light extraction at the main emission wavelength of europium chelates (619 nm). David *et al* reported that a 2D geometry is notably more efficient to extract guided modes than a 1D patterning [15]. They also calculated that the choice of the 2D lattice shape (triangular, square, etc) does not substantially change the extraction efficiency for still modest indices as those used here. We thus choose in this study a simpler square geometry. The resulting depth of the imprinted PhC is 40 nm,

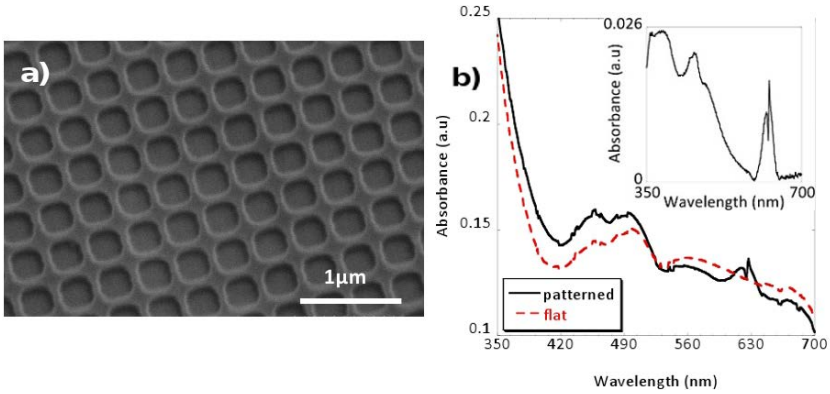

Figure 2. (a) SEM micrograph of the top surface grating. (b) Apparent normal incidence absorbance spectrum of the patterned (line) and flat (dots) areas of the sample. The inset shows the difference between the two curves. The peaks around 600 nm are due to resonant guided mode excitation.

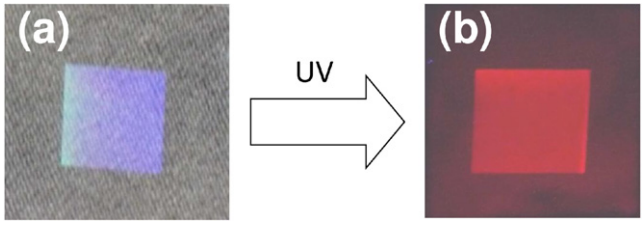

Figure 3. Photograph of the sample under (a) daylight and (b) UV excitation. The patterned area is the square made visible by using grating diffraction using daylight from a nearby window. This area appears brighter in (b), showing the predominant role of the patterning on red emission extraction.

as deduced from AFM measurements, which is smaller than the master PhC depth. Note that the reproducibility of the mask structure onto the imprinted film could probably be improved through adjustment of the sol chemistry conditions [16] but it is beyond the purpose of this work. AFM measurements also confirm the 400 nm period. This period has been chosen for efficient outcoupling, the main emission peak of the europium chelate being extracted close to the normal of the sample ($\theta = 0°$). We check this directly by performing standard absorbance measurements for normally incident light, resulting in the spectrum shown in figure 2(b). The inset in this figure shows the difference between absorbance of flat and patterned sample areas. Two peaks are seen in the absorbance spectrum of the patterned area between 600 and 650 nm (i.e. two dips in transmission). They are attributed to the resonant excitation of the TE and TM guided modes, respectively. Note that this can be seen as a Wood or Fano anomaly, well known in the context of diffraction gratings [17]. For other wavelengths, only expected variations mainly due to thickness modulations between patterned and flat areas are visible. In particular, there is no significant feature around 376 nm, which would entail an enhancement of excitation coupling. In the first approximation, the properties of these guided modes can be calculated with a one-dimensional mode solver [18] replacing the 40 nm thick PhC layer by a lower average refractive index $n_{\mathrm{av}} = (n_{\mathrm{film}}^2(1-f)+f)^{1/2}$.

The enhanced extraction effect provided by the PhC is obvious when placing the sample under a UV lamp to excite the europium emission. In the photographs presented in figure 3, the 5 × 5 mm patterned area appears brighter than the surrounding unpatterned area, whereas they contain the same density of luminescent molecules, that of the initial core luminescent sol–gel (see figure 1).

The role of the PhC at the surface is to outcouple the guided light which spectrally and spatially overlaps its modes. Without patterning, photons remain guided into the luminescent layer (figure 4(a)), whereas with the PhC, the guided light is extracted via leaky modes to free space, as presented in figure 4(b).

2.2. Introduction of a porous intermediate layer

With a strong coupling between the PhC and the guided modes, and no losses by scattering effects, all the guided light should be extracted by the PhC. Nevertheless, when luminescent slabs are deposited onto glass substrates, a non-negligible part of the light is emitted from the film and trapped into the substrate. In order to rein in these losses and purposely increase the fraction of emitted light which is guided in the luminescent layer itself, a low refractive index porous silica layer is introduced between the substrate and the luminescent layer (figures 1(b) and 4).

Elaboration of these low refractive index porous layers was achieved according to the procedure developed by Guillemot *et al* [13]. The porous fraction is controlled using templating poly(methyl methacrylate) (PMMA) latex nanoparticles with a mean diameter of 60 nm that are incorporated into a silica sol before spin-coating on the glass substrate. As the luminescent molecules are damaged at high temperature, the 60 nm latex nanoparticles have to be removed by calcination before the luminescent layer deposition. In order to prevent the luminescent solution from collapsing into the pores during deposition, a very thin flat layer of dense silica is added onto the porous film before calcination and removal of the latex filling the pores. This layer has to be thin enough to cause negligible perturbation of the optical path. The elaboration technique is detailed in section 6. The present study investigates the effect of this intermediate layer on the PhC extraction of the luminescence described above for different porosity factors. The porous fraction of this layer, and thus its refractive index, is controlled by adjusting the latex

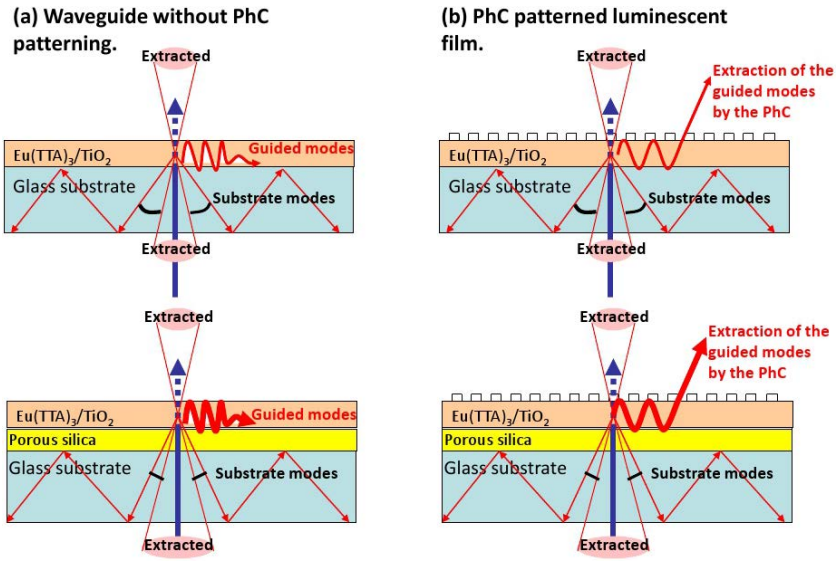

Figure 4. Fate of the emitted light (a) without patterning of the surface and (b) with PhC at the surface. Samples without (top) and with an intermediate porous silica layer (bottom) are represented. A small fraction of the emitted light is directly emitted in the air cone. Another part is guided in the layer and can be extracted from the layer in the presence of a PhC only. The third fraction is extracted to the substrate, guided and not visible from the top of the device. The intermediate porous layer helps to diminish this fraction of light emitted to the substrate.

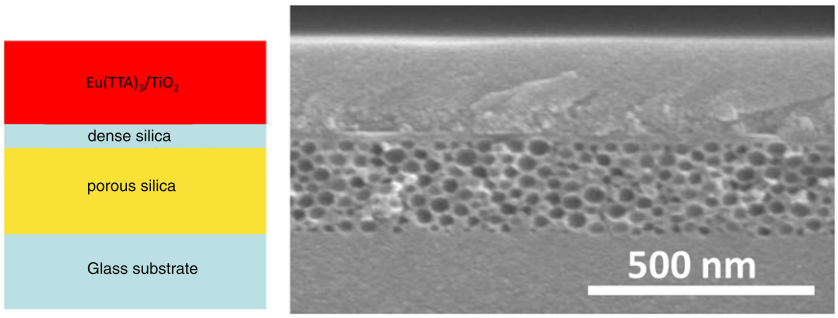

Figure 5. SEM photograph of the luminescent film cross section deposited onto a low-index porous layer.

volume fraction in the initial precursor solution [13]. Figure 5 shows the direct observation by SEM of a sol–gel film cross section, prior to patterning, when deposited onto the porous intermediate layer, with an intermediate thin planarization layer of dense silica between porous silica and titania film.

As the refractive index of the porous layer is lower than the glass one, the refractive index difference between the luminescent layer and the layer underneath increases. This modifies the relative repartition of light: extracted to air, trapped inside the luminescent layer or the substrate (figure 4). The light guided in substrate modes is lost and does not contribute to the film emission. By reducing the extraction cone to the substrate, the porous layer diminishes this fractional leakage contribution.

2.3. Effect on the excitation path

The introduction of the porous layer also diminishes the bounces of the UV excitation light inside the substrate. Figure 6 presents two luminescent patterned slabs with (a) and without (b) an intermediate porous layer. For the sample deposited onto the substrate, extra spots are visible along both 0° and 45° sets of directions. These spots stem from the diffraction of UV light by the PhC bouncing on the bottom face of the glass before again exciting the luminescent layer (see figure 6(c)). For each set (0° or 45°), the diffracted beam travels in the glass under a specific inclination i, related to the PhC period along each set (in other words, related to the direction-dependent distance to the first Brillouin zone boundary). In the presence of the porous layer, whereas UV light undergoes the same fate for the 0° set of four directions, for the other set (45°), the in-plane wavevector of diffracted light is larger than $k_0 \times n_{\text{porous}}$ but does not correspond to a guided mode either. Thus, no scattering occurs due to these 45° reciprocal vectors and the corresponding spots are lost (see figures 6 (b) and (d)). Optical tunneling through the porous layer is negligible given its 200 nm thickness. The porous layer is therefore beneficial to optical measurement because its presence diminishes parasitic light originating from the multiple spots of the laser beam.

In this first part, the structure of the model system has been presented. Through basic experiments, we indicated why the chosen sample features (PhC parameters, porous buffer layer, etc) are favorable for the extraction of the emitted light. The

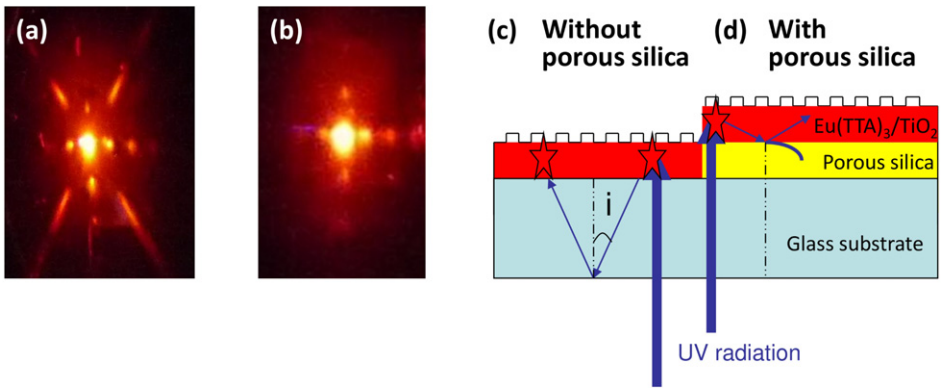

Figure 6. (a) and (b) photographs of luminescent slabs excited by the UV laser deposited on glass (a) or porous intermediate buffer layer (b). (c) and (d) are the corresponding schematics.

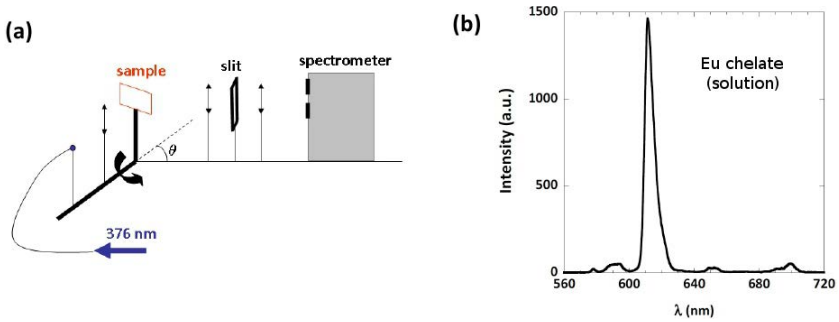

Figure 7. (a) Sketch of the set-up with rotating stage. (b) Typical emission spectrum of the europium chelate in solution.

porous intermediate layer is beneficial as it also increases the part of the light which is guided and then potentially extracted by the PhC. We will now focus on the fate of the guided light.

3. Angle-resolved luminescence measurements

3.1. Measurement principle

To characterize in more detail how the PhC modifies the far-field emission, we resort to an angle-resolved luminescence set-up along a single direction presented in figure 7(a). In this set-up, the UV excitation laser is first injected into a fiber whose end lies on an excitation stage which rotates around a vertical axis. On this stage, the fiber end is focused with a lens ($f = 16$ mm) on the sample, at a point which is finely adjusted on the rotation axis, the sample holder being nevertheless on the same stage.

The excitation is interdependent with the sample, thus stable, constant and independent from the angle of the stage. The spectrometer, fixed on the table, collects and analyzes the signal during the stage rotation, through a first lens ($f = 200$ mm) creating a parallel beam, and a second one focusing the image of the excitation spot onto the spectrometer slit (50 μm width). We insert an extra 1 mm wide vertical slit located at the focal plane of the first lens. This slit performs a narrow **k**-selection in the horizontal plane, so that the collected intensity is termed $I(\theta, \lambda)$. It aims at quick acquisitions that provide a fair angular resolution (5 mrad $\sim$ 0.3°) without losing too much signal, as would be the case with a standard pinhole. We will see later how the absence of **k**-selection in the vertical direction impacts the detection of the various extraction channels.

The intrinsic emission spectrum of the europium chelate is shown in figure 7(b). It was measured in solution to avoid any microstructure effect. Of interest for us will be the two peaks at 594 and 600–630 nm. Figure 8(a) presents the collection of several spectra measured at various emission angles (typically with a 0.2° step) as a two-dimensional color map $I(\theta, \lambda)$ of emission versus angle and wavelength for the patterned sample. The extraction is enhanced along the diffraction band corresponding to the chosen PhC pattern so that the emission spectrum is expected to be modulated for each angle. The inset of figure 8(a) shows as an example the angular dependence of the intensity emitted at one of the europium emission peak (594 nm). By changing the 2D map to a map of emission vs. guided wavevector and frequency $I(k, \omega)$, these bands shall appear as the folded dispersion bands of the PhC.

We also developed a simple model to reproduce the main features (lines and 'fraction of disc') of emission of luminescent layers patterned with a square lattice PhC. Figure 8(b) represents the resulting 2D luminescence map for this emission model of the PhC slab, to be compared to that of figure 8(a). The basis is the conservation of momentum between waveguide modes and free-space modes, within a reciprocal vector **G**. The theory is detailed at the end of this paper. The comparison of the calculated and measured 2D maps allows the determination of the effective refractive index of the guided modes. For a period of 400 nm measured by

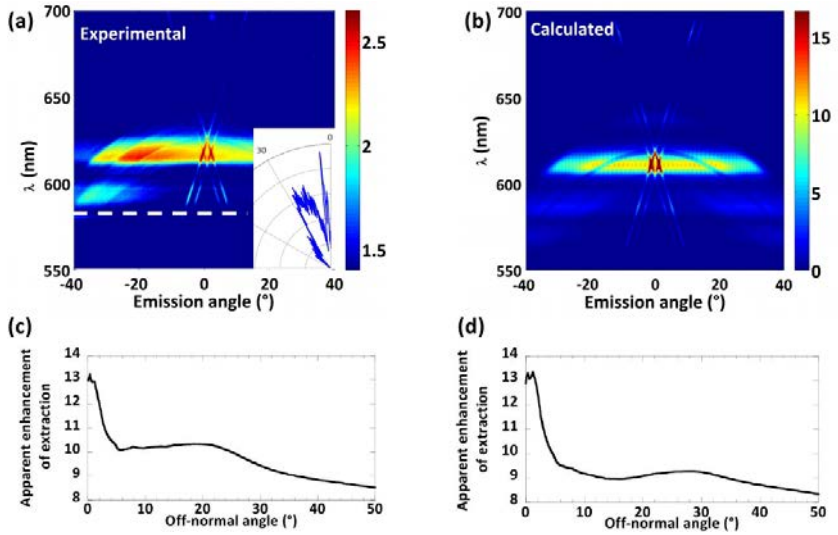

Figure 8. (a) 2D map of the luminescence for the PhC slab. This plot is obtained by collecting spectra at stepped angles between 0 and 180°. It is limited here to the range [−40°:40°] because no luminescence is visible beyond this angle range. Inset: section of the 2D map at one of the europium peaks (594 nm, dashed line) in polar form, showing the highly directional features. (b) Calculated 2D map of luminescence for the PhC slab. (c) Experimental extraction enhancement factor adapted to our set-up as a function of the half-angle of the integration cone. (d) Theoretical extraction enhancement factor as a function of the half-angle of the integration cone (normalized so that the calculated signal matches the experimental one at 50°).

SEM and AFM, the experimental data (figure 8(a)) match our model for effective indices $n_{\mathrm{TE}} = 1.55$ and $n_{\mathrm{TM}} = 1.53$ for TE and TM modes, respectively (figure 8(b)). This is consistent with the calculated values [18] using the period $a =$ 400 nm, the refractive index of the waveguide characterized by ellipsometry ($n = 1.65$) and the above average index $n_{\mathrm{av}} = 1.5$ for the PhC.

We get a first approach of extraction enhancement from the comparison of emission signals from the patterned and flat areas, integrating them over the main peak (619 ± 13 nm) from angle $-\theta$ to angle θ. These integrated signals are respectively labeled $J_{\mathrm{PhC}}(\theta)$ and $J_{\mathrm{flat}}(\theta)$. We calculate the ratio $J_{\mathrm{PhC}}/J_{\mathrm{flat}}$ and get the graph of figure 8(c). The enhancement ratio obtained will be discussed later in the fourth section but the typical value of 8 can be retained over a numerical aperture (NA) of 0.77 ($\theta = 50°$). We also calculate the ratio $J_{\mathrm{model}}/J_{\mathrm{flat}}$, where J_{model} is calculated taking as the patterned area the 2D map of the optical model normalized so that, at 50°, $J_{\mathrm{model}}(50) = J_{\mathrm{PhC}}(50)$. Figure 8(d) reports the ratio $J_{\mathrm{model}}/J_{\mathrm{flat}}$. As the model is normalized, only the shape of both curves (figures 8(c) and (d)) can be compared and not the absolute value.

3.2. Optical results for the model system deposited on porous layer

Figure 9 shows 2D luminescent maps for porous layers of 10% (a), 25% (b), 50% (c) and 70% (d) porous fractions. The porous layers present a disorder, which does not affect the existence of guided modes inside the layer, at least at small porosity factors, as shown in the experimental 2D map of luminescence (figures 9(a) and (b)). It means that scattering effects are not dominant, partly due to the presence of the thin dense silica layer, which plays a planarization role and to the subwavelength size of the buffer layer pores (60 nm). The insertion of the porous layer has an impact on the 2D luminescence map $I(\theta, \lambda)$: it first diminishes the effective indices n_{TE} and n_{TM}, and thus shifts the mode crossing of figure 8 to shorter wavelengths. Next, it increases the modal birefringence $n_{\mathrm{TE}} - n_{\mathrm{TM}}$. Table 1 reports the refractive index n_{porous} of the porous layers and the evolution of n_{TE} and n_{TM} when the porosity increases, obtained by adjusting our simulations with experimental 2D luminescence maps. At a 50% porous fraction (figure 9(c)), the TM mode appears as a dip on the 2D luminescent map for wavelengths above 590 nm, although some traces of this mode are still visible for shorter wavelengths. The TE mode turns out to be unaffected. At a 70% porous fraction, the TM mode disappears completely. We will discuss the plausible cause of this TM disappearance in section 4.

Table 1. Experimental values of n_{porous}, n_{TE} and n_{TM} for different porous fractions.

Porous fraction (%)	n_{porous}	n_{TE}	n_{TM}
0	1.5	1.548	1.528
10	1.42	1.538	1.508
25	1.36	1.535	1.49[a]
50	1.25	1.528	No guided mode
70	1.16	1.520	No guided mode

[a] No guided mode found with the 1D mode solver, TM mode visible experimentally only for wavelengths below 600 nm.

4. Discussion

As presented in section 3, the comparison of calculated and measured 2D maps provides the guided-modes effective

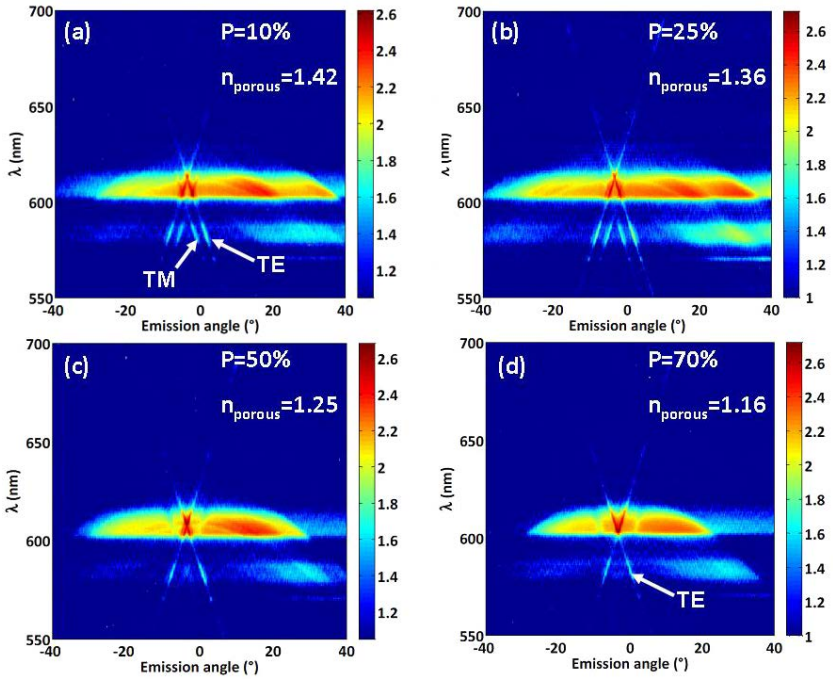

Figure 9. 2D map of the luminescence for the PhC slab deposited on the porous silica layer presenting various porous fractions: (a) 10%, (b) 25%, (c) 50% and (d) 70%.

indices. The isotropic guided emission assumption means that, in k-space, the guided mode at each emitted wavelength spans a circle of radius k. The square PhC leads to the translation of this k-space circle in the four directions by vectors $\mathbf{G}$ associated with the lattice, here the four first vectors. The diffraction by the two horizontal $\mathbf{G}$'s is collected nearly exclusively through a vertical tangent arc fully comprised in the slit (see figure 11 of section 6.2.1 in k-space). It leads to the usual diffraction band pair seen in figure 8(a). They presently cross at almost normal incidence because our $\mathbf{G}$ modulus is nearly matched to the guided wavevector modulus $k = (2\pi/\lambda)n_{\text{eff}}$. The less intuitive result is the large background with the shape of a truncated thick ring, which is due to the extraction by the vertical $\mathbf{G}$'s, whose collection is allowed by the elongated shape of the slit in the vertical direction. Such a process provides signals on a broad θ range, namely as long as the slit intersects the vertically shifted circles (see figure 11 of section 6.2.1 in k-space). The range in question is thus obviously wavelength-dependent.

On the experimental $I(\theta, \lambda)$ map (figure 8(a)), one shadow line, crossing the TE mode at $\theta = 0$, is visible. This is the signature of the in-plane second-order distributed feedback, well known in the framework of coupled mode theory [19]. The distributed feedback effect in the waveguide plane corresponds to the Bragg relation $k' + 2\mathbf{G} = k$ verified at the crossing of two circles as presented in the scheme of section 6.2.2. Note that both circles are along the same direction, y here, and correspondingly the signatures we observe relate essentially to one-dimensional periodicity. Profoundly, the emission process itself is modified at such crossings, the coupling between guided modes leading to a small forbidden band in the corresponding directions and wavelengths. It is well known that, within a photonic bandgap, the optical mode density is reduced and therefore emission is reduced in such bandgap spectral ranges [20].

Kazarinov introduced two coupling constants h_1 and h_2 to characterize first-and second-order feedback of a periodic structure [19a]. h_1 is the grating coefficient describing scattering while h_2 describes the reflection of the guided wave. In his study of DFB lasers with asymmetric mark–space ratio, a large feedback coefficient h_2 is expected with comparatively weaker radiation losses h_1. For an efficient emitting luminescent PhC slab, as h_1 is a signature of the out-of-plane diffraction strength, related to the inverse of the extraction length, h_1 has to be much higher than h_2, which is related to the forbidden bands. In our case, we do not completely extinct h_2 as proven by the presence of the shadow line on the 2D map of luminescence (figure 8(a)), although h_2 is very small ($h_2 < 3$ cm^{-1}) if calculated by the Kazarinov equation from a 1D projection of our PhC parameters. The feedback effect remains nevertheless noticeable when it is allowed by momentum conservation. Using our guided mode and corrugation profiles, h_1 is evaluated from [19a] to be 3.6×10^{-3} μm^{-1} $= 36$ cm^{-1}, leading to a characteristic extraction length of 140 μm. In the present PhC configuration ($f = 0.26$), the ratio h_1/h_2 described by the Kazarinov equations for an equivalent 1D projection reaches nearly its maximum, hence the small upper bound for h_2 given above. Thus the filling factor used in this study is well adapted to the period of 400 nm chosen to extract the main europium emission peak (612 nm). When a and f are fixed, the extraction length also depends on other parameters. To obtain a shorter extraction length, i.e. to extract more efficiently the guided light, the corrugation depth especially needs to be increased. An adaptation of the imprint technique to match the depth of the mask's corrugation could help in reaching shorter extraction lengths.

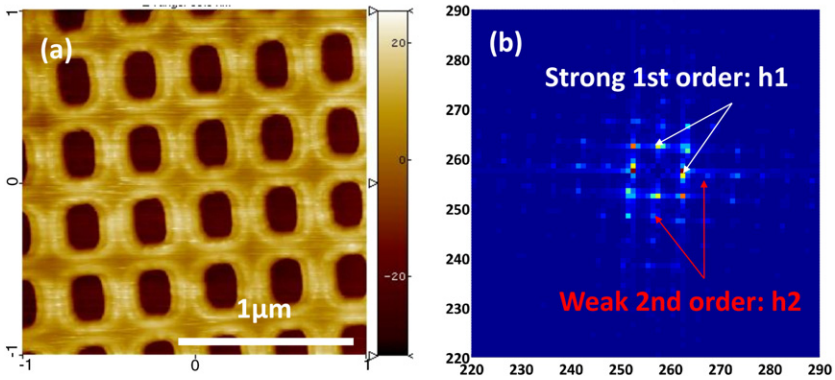

Figure 10. (a) AFM profile of the patterned luminescent film and (b) Fourier transform of the AFM profile; qualitative analysis of the ratio h_1/h_2.

The knowledge of diffraction strength of the PhC can also benefit from a 2D approach. Calculation of the 2D Fourier transform of the PhC dielectric map directly gives 2D information on its photonic strength, in other words on the ability of harmonics to diffract light. Figure 10 presents the corrugation profile measured by AFM and the corresponding Fourier transform. The ratio between first-and second-order Bragg peaks is evaluated to more than 100 on the Fourier transform plot by integrating the first-and second-order peaks, respectively, which is consistent with the high expected value of h_1/h_2.

Figure 8(c) presents the enhancement factor for the main emission wavelength of the europium chelate when integrating between $-\theta$ and θ. We estimate an accuracy of only 20% due to the weak absolute signal and the associated offset sensitivity. The small-angle peak reaching around 13 is related to the near-normal extraction of horizontally shifted circles (figure 11). The plateau at a ratio of about 10 and at angles ranging from about 7° to 20° rather comes from the vertically shifted circles (figure 11 of section 6.2). At larger angles, a typical value of 8 can be retained. Towards 90°, the enhancement progressively diminishes. Note that the specific geometry prevents us comparing these data ($J_{\mathrm{PhC}}/J_{\mathrm{flat}}$) with extraction from a limited NA in the standard sense of a disc in k-space, given our specific limit on vertical angle $\theta_y < \theta_{y\,\max}$. The only case where this applies well is for θ values such as $\theta_{x\,\max} = \theta_{y\,\max}$: in this case, we integrate over a square of k-space, which should give a result very close to a circle in k-space. Thus the values of about 10 are correct for this small NA. Overall, the extraction appears to be efficient. The picture of extraction of guided modes by the PhC is essentially correct. It is thus logical to expect that the introduction of porous buffer layers would increase the fraction of light guided in the luminescent layer and potentially extracted and would lead to brighter luminescent films.

The characterization of samples deposited on porous layers leads to the same superposition of the usual diffraction lines due to the horizontally shifted circles with a large truncated thick ring, as a signature of the vertically shifted wavevector circles. As n_{porous} decreases, n_{TE} and n_{TM} decrease. The existence of the TE mode turns out to be unaffected by the porous layers even for high porous fractions, whereas the TM mode disappears for porous fractions higher than

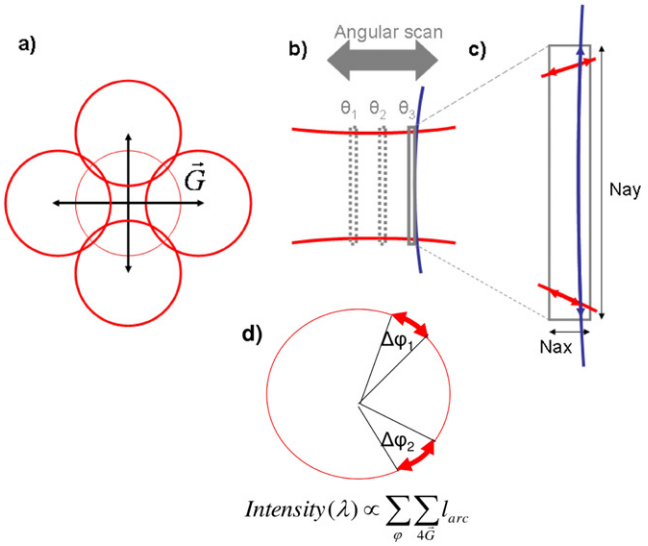

Figure 11. (a) Model for the slit selection of luminescence PhC extraction channels, here at one particular wavelength; (b) and (c) the slit intersects up to four translated circles from grating vectors **G** and (d) each intersect has an angular range $\Delta\varphi$ adding to PhC-extracted light.

50% (figure 8). In this configuration, the porous layer presents a finite thickness ~200 nm. As a basis to discuss the disappearance of the TM mode, we note that the basic calculation for a luminescent film deposited on a very thick porous substrate ($n_{\mathrm{porous}} = 1.25$, for example) finds a TM mode at $n_{\mathrm{TM}} = 1.47$ whereas no bona fide TM mode is found if the whole stack is taken into account (dense silica thin layer but mainly finite porous layer and glass substrate). In the calculation with a thick porous substrate, we have just shown that a TM mode is found, presenting an effective index close to the glass refractive index. Thus a thicker porous layer could help keeping the TM mode emission and recover this contribution in the light emitted out of the layer. It is thus seen that the approach of a porous layer first necessitates knowledge of the impact of the porosity itself on the very existence of guided mode versus leakage and scattering. Notably a quantitative analysis is awkward without such prior knowledge.

5. Conclusion

The context of this work is the development of optimized light-converting phosphor layers for lighting or display devices. The basic idea is to understand and control the material microstructure and dielectric properties, two parameters that determine light propagation phenomena. In this work, we focused our attention on a model system consisting in red-emitting europium chelate homogeneously dispersed within a titania sol–gel matrix. This allows us to mimic converter layers that could be used, for example, in white LEDs without having any uncontrolled diffusion from the phosphor grains.

Considering our europium-chelate-doped titania film, we focused our attention on the effect of a 2D photonic structure obtained by soft nanoimprint lithography (S-NIL): an enhancement of about a factor of eight is observed for patterned films, which shows that all the guided light is extracted. To get brighter luminescent films, the introduction of a low refractive index porous sublayer offers the opportunity to reduce the light leaking into the substrate and increase the fraction of light guided in the luminescent layer and potentially extracted. However, we showed that a better knowledge was required to take the benefit of this approach. We show that a single-angle technique is a quick and simple alternative to 2D angular spectroscopy or to m-line techniques for waveguide and extraction investigations, capitalizing successfully on the analysis of PhC diffraction. The extraction from luminescent phosphors by patterned slabs is controlled by the existence and nature of guided modes, and how they experience the various extraction channels, scattering inside the core and cladding. These experiments on a model system using a molecular-like emitting system opens the way towards the development of films with an optimized microstructure, based on the much more relevant inorganic phosphor that should be considered, such as dispersed nanoparticles to avoid random light diffusion effects and simultaneously take the benefit of a predictive strategy for down-converting.

6. Experimental details

6.1. Sample preparation

6.1.1. Luminescent layer. The sol–gel method consists in depositing films from a liquid solution containing TiO_2 molecular precursors (called a 'sol') that can be converted into amorphous or nanocrystalline TiO_2 after a thermal treatment. Titania sol is prepared by mixing titanium (IV) butoxide (18 ml) with butanol (9.8 ml) during 10 min. Then, acetic acid (27.3 ml) is added and the mixture is heated at 50 °C. After 30 min, the solution is cooled to 0 °C with ice during 1 h. DI water (8.9 ml) and ethanol (37.6 ml) are mixed together and added drop by drop in the cold solution. The resulting mixture is heated at 50 °C for 1 h. The solution is stirred during all steps of the synthesis. Finally, the sol is filtered with a 0.22 μm porous membrane.

Europium complexes $Eu(TTA)_3$ are synthesized following the process previously described by De Silva *et al* [21]. The product is dissolved in the titania precursor solution (20 mg ml^{-1}). After 10 min of stirring, the solution is limpid. The films are deposited onto glass substrates by spin-coating (2000 rpm, 30 s). The wafers were previously cleaned by 20 min immersions in a fresh piranha solution (H_2O_2 (30%)/H_2SO_4 1:3 vol). This easy in-house elaboration technique gives access to various refractive indices and film thicknesses, depending on the dilution of the sol and the post-deposition thermal annealing. These parameters can be measured by ellipsometry. As described previously, without annealing, the refractive index of the resulting film is $n = 1.65$. It increases to $n = 2$ after annealing at 400 °C, which is closer to the GaN refractive index ($n = 2.3$). Nevertheless, this annealing induces crystallization of the matrix, which leads to scattering of light due to grain boundaries and damage of the luminescent complexes. We thus study here films dried at 110° but not crystallized. The thickness of the resulting film is typically around 200 nm before annealing. This value can be decreased by dilution prior to deposition or increased by prior evaporation of part of the solvent before deposition.

6.1.2. NIL. A silicon mold is patterned with the chosen architecture by electron beam lithography. With a single silicon mold, we obtain several polydimethylsiloxane (PDMS) negative replica by casting. The periodic pattern of the PDMS mold is transferred to the TiO_2 sol–gel film by soft nanoimprint lithography [14]. A TiO_2 precursor solution is spin-coated onto the film. Before condensation of the gel, an anti-adhesive-treated PDMS mold is deposited on it. The system is heated at 110 °C under pressure (20 PSI) during 5 min in an NXR2500 imprinter from Nanonex. During this step, the viscous sol fills the voids of the mold and becomes solid because of the polymerization of the titania network induced by warming. After cooling, patterned films were easily separated from the stamp.

6.1.3. Porous layer. Porous silica thin films are prepared through a conventional sol–gel process using sacrificial organic templates following the method reported by Guillemot *et al* [13]. As the luminescent molecules are damaged by calcination, the 60 nm latex nanoparticles have to be removed before the luminescent layer deposition. In order to prevent the luminescent solution from collapsing into the pores during deposition, a very thin flat layer of dense silica is added onto the porous film before calcination and removal of the latex filling the pores. This layer has to be thin enough to cause negligible perturbation of the optical path. A diluted silica solution presenting a solid content of 1% leads to a 20 nm thick silica layer. The presence of latex molecules in the porous film assists the adhesion of the film during deposition, preventing it from dewetting. This silica layer also plays a planarizing role. The sample is then calcinated slightly above 400 °C to remove the latex and drain the porosity. In this study, the porous film thickness is kept constant and films are 200 nm thick, whatever their porous fraction. The porous fraction of the resulting film is controlled by adjusting the latex volume fraction in the precursor solution. Films of porosity from 10 to 75% are deposited on glass substrates. Porosity and thicknesses are checked by ellipsometry.

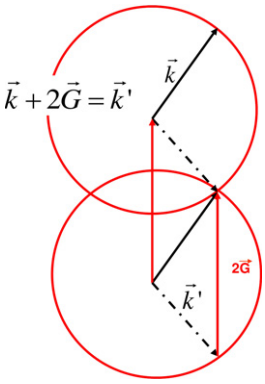

Figure 12. Schematic of the Bragg condition.

After this step, the luminescent layer is deposited above the porous intermediate layer.

Finally, the resulting luminescent slab is patterned by soft nanoimprint lithography as described previously.

6.2. Optics: theoretical model

6.2.1. Vertical and horizontal contribution to the extraction. Our main scope here is to take advantage of the reasonable assumption that guided light is essentially evenly distributed along the azimuth φ of the plane, assuming the periodicity to act only on the scattering of this guided light, and neglecting first the formation of in-plane forbidden bands. Then, this angle is the good underlying variable. Thus our model consists in scanning the wavelength and further the angle φ (angle in the waveguide plan) to evaluate which angular range $\Delta\varphi$ of guided wave wavevectors **k** are outcoupled in the angular detection slit through the fundamental reciprocal vectors **G** of the lattice. The procedure is applied successively for both polarizations.

In figure 11, the isotropic guided emission assumption means that in **k**-space, the guided mode at each emitted wavelength spans a circle of radius k (the thin line in figure 11(a)). The square PhC leads to the translation of this circle in the four directions by the vectors **G** associated with the lattice ($\mathbf{G} = 2\pi/a$, circles of thick lines in figure 11(a)). For this wavelength, at a direction θ selected by the slit, the extracted intensity is proportional to the cumulative arcs of the four circles included in the slit, neglecting interferences among the optical paths (only occurring at the circle intersections). The slit of physical width $d_x \times d_y$ is represented by two numbers NA_x and NA_y characterizing its narrow and large dimensions, respectively. The scheme in figure 11 summarizes the situation and depicts the variables involved. The narrow one is, of course, scanned when rotating the detection angle θ. Reasoning in the frame of the sample, the collected directions are within horizontal angles $\theta \pm \Delta\theta$, with $\Delta\theta = \mathrm{NA}_x/2 = d_x/(2f)$. The vertical angle spans a symmetrical range $\pm\mathrm{NA}_y/2 = \pm d_y/(2f)$. The amount of collected light through the extraction of guided modes is then, for each **G**, proportional to the length of the corresponding arc intercepted by the aperture (figures 11(b)–(d)).

6.2.2. Distributed feedback effect. This feedback effect (figure 12) occurring at the circle intersection as discussed above is taken into account phenomenologically in the simulation presented previously by an ad hoc modulation of the intensity, specifically a reduction for a small window around the exact Bragg condition.

Acknowledgments

We thank Dr Fouad Maroun for his help on AFM measurements and Anne Lelarge for SEM measurements. Dr Lucio Martinelli is also acknowledged for valuable discussions.

References

[1] Ko K-Y, Lee Y K, Park H K, Kim Y-C and Do Y R 2008 *Opt: Express* **16** 5689
Sohn K-S, Shin N, Kim Y-C and Do Y R 2004 *Appl. Phys. Lett.* **85** 55
[2] Schnitzer I, Yablonovitch E, Caneau C, Gmitter T J and Scherer A 1993 *Appl. Phys. Lett.* **63** 2174
[3] Fan S, Villeneuve P R, Joannopoulos J D and Schubert E F 1997 *Phys. Rev. Lett.* **78** 3294
[4] David A, Fujii T, Sharma R, McGroddy K, Nakamura S, DenBaars S P, Hu E L, Weisbuch C and Benisty H 2006 *Appl. Phys. Lett.* **88** 061124
[5] Do Y R, Kim Y C, Song Y W, Cho C O, Jeon H, Lee Y J, Kim S H and Lee Y H 2003 *Adv. Mater.* **15** 1214
[6] Mele E, Di Benedetto F, Persano L, Cingolani R and Pisignano D 2005 *Nano Lett.* **5** 1915
[7] Ganesh N, Zhang W, Mathias P C, Chow E, Soares J A N T, Malyarchuk V, Smith A D and Cunningham B T 2007 *Nature Nanotechnol.* **2** 515
[8] Diana F S, David A, Meinel I, Sharma R, Weisbuch C, Nakamura S and Petroff P M 2006 *Nano Lett.* **6** 1116
[9] Lemarchand F and Rigneault H 2002 *J. Opt. A: Pure Appl. Opt.* **4** S115–8
[10] Persad A, Chow K-F, Wang W, Wang E, Okafor A, Jespersen N, Mann J and Bocarsly A 2008 *Sensors Actuators* B **129** 359
[11] Sanchez C, Lebeau B, Chaput F and Boilot J-P 2003 *Adv. Mater.* **15** 1969
[12] Di Benedetto F, Biasco A, Pisignano D and Cingolani R 2005 *Nanotechnology* **16** S165
[13] Guillemot F, Brunet-Bruneau A, Bourgeat-Lami E, Gacoin T, Barthel E and Boilot J-P 2010 *Chem. Mater.* **22** 2822
[14] Cattoni A, Cambril E, Decanini D, Faini G and Haghiri-Gosnet A M 2010 *Microelectron. Eng.* **87** 1015
Truong T A, Campos L M, Matioli E, Meinel I, Hawker C J, Weisbuch C and Petroff P M 2009 *Appl. Phys. Lett.* **94** 023101
[15] David A, Benisty H and Weisbuch C 2007 *J. Disp. Technol.* **3** 133
[16] Hampton M J, Williams S S, Zhou Z, Nunes J, Ko D-H, Templeton J L, Samulski E T and DeSimone J M 2008 *Adv. Mater.* **20** 2667
[17] Fano U 1941 *J. Opt. Soc. Am.* **31** 213
[18] wwwhome.math.utwente.nl/∼hammerm/oms.html
[19a] Kazarinov R F and Henry C H 1985 *IEEE J. Quantum Electron.* **21** 144
[19b] Benisty H, Danglot J, Talneau A, Enoch S, Pottage J M and David A 2008 *IEEE J. Quantum Electron.* **44** 777
[20] Yablonovitch E 1987 *Phys. Rev. Lett.* **58** 2059
[21] De Silva C R, Maeyer J R, Wang R, Nichol G S and Zheng Z 2007 *Inorg. Chim. Acta* **360** 3543